

Performance of ePix10K, a High Dynamic Range, Gain Auto-Ranging Pixel Detector for FELs

G. Blaj^{1,a)}, A. Dragone¹, C. J. Kenney¹, F. Abu-Nimeh¹, P. Caragiulo¹,
D. Doering¹, M. Kwiatkowski¹, B. Markovic¹, J. Pines¹, M. Weaver¹, S. Boutet¹,
G. Carini^{1,2}, C.-E. Chang¹, P. Hart¹, J. Hasi¹, M. Hayes¹, R. Herbst¹, J. Koglin¹,
K. Nakahara¹, J. Segal¹ and G. Haller¹

¹SLAC National Accelerator Laboratory, 2575 Sand Hill Road, Menlo Park, CA 94025, U.S.A.

²Currently at Brookhaven National Laboratory, Upton, NY 11973, U.S.A.

^{a)}Corresponding author: blaj@slac.stanford.edu

Abstract. ePix10K is a hybrid pixel detector developed at SLAC for demanding free-electron laser (FEL) applications, providing an ultrahigh dynamic range (245 eV to 88 MeV) through gain auto-ranging. It has three gain modes (high, medium and low) and two auto-ranging modes (high-to-low and medium-to-low). The first ePix10K cameras are built around modules consisting of a sensor flip-chip bonded to 4 ASICs, resulting in 352×384 pixels of $100 \mu\text{m} \times 100 \mu\text{m}$ each. We present results from extensive testing of three ePix10K cameras with FEL beams at LCLS, resulting in a measured noise floor of 245 eV rms, or $67 e^-$ equivalent noise charge (ENC), and a range of 11 000 photons at 8 keV. We demonstrate the linearity of the response in various gain combinations: fixed high, fixed medium, fixed low, auto-ranging high to low, and auto-ranging medium-to-low, while maintaining a low noise (well within the counting statistics), a very low cross-talk, perfect saturation response at fluxes up to 900 times the maximum range, and acquisition rates of up to 480 Hz. Finally, we present examples of high dynamic range x-ray imaging spanning more than 4 orders of magnitude dynamic range (from a single photon to 11 000 photons/pixel/pulse at 8 keV). Achieving this high performance with only one auto-ranging switch leads to relatively simple calibration and reconstruction procedures. The low noise levels allow usage with long integration times at non-FEL sources. ePix10K cameras leverage the advantages of hybrid pixel detectors with high production yield and good availability, minimize development complexity through sharing the hardware, software and DAQ development with all other versions of ePix cameras, while providing an upgrade path to 5 kHz, 25 kHz and 100 kHz in three steps over the next few years, matching the LCLS-II requirements.

INTRODUCTION

Free-electron lasers (FELs), with their unmatched combination of x-ray laser pulses with energies (in the order of keV), time scales (in the order of femtoseconds), brilliance (10^{12} to 10^{13} 8 keV photons) and coherence, similar to energy and time scales of atoms and molecules, enabled a new era of imaging the motion of atoms and molecules and the dynamics of chemical reactions. Currently there are four hard x-ray Free-Electron Lasers (FELs) operating worldwide: LCLS (2009) [1], SACLA (2011) [2], PAL-XFEL (2016) and EuXFEL (2017), with several more facilities planned to open in the near future (e.g., SwissFEL).

The short, high brilliance x-ray pulses at FELs are resulting in unique constraints on detectors: low noise, high range, good linearity, low cross-talk, high acquisition rates, detection of large numbers of photons entering the sensor within femtoseconds [3], and modularity for facilitating repairs [4]. Typical FELs operate at 60 Hz to 120 Hz, while next generation FELs are planned to operate at much higher pulse rates: EuXFEL at 27 000 pulses/s [5] and LCLS-2 gradually ramping up to 10^6 pulses/second [6], thus requiring a path towards high repetition rate detectors.

CSPAD detectors have been workhorse detectors at LCLS since the start in 2009, with tens of megapixels deployed in multiple cameras, and tens of petabytes of data collected [7, 8, 9, 10]. The ePix family represents a new generation of detectors developed at SLAC, greatly increasing all relevant parameters (noise, range, linearity, cross-talk) while offering an upgrade path towards 5 kHz and beyond [11]. The ePix100 detectors offer low noise ($43 e^-$

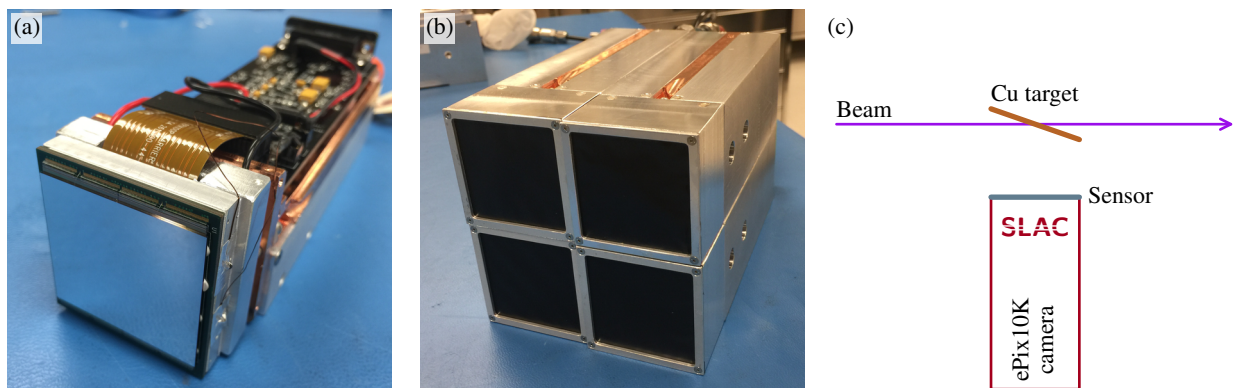


FIGURE 1. (a) Typical (vacuum compatible) ePix camera with covers removed, showing the large 35.2 mm \times 38.4 mm sensor with 4 read-out ASICs; (b) the first four ePix10K cameras; (c) top view schematic diagram of the experimental setup used for gain calibration, linearity testing, flat field and imaging tests; objects for imaging were inserted between the Cu target and the sensor.

equivalent noise charge, ENC, or 155 eV rms [12]) and range of 100 8 keV photons, with 12 cameras (0.5 megapixels each) deployed between 2015 and 2018 at LCLS [13] and 4 cameras deployed at the EuXFEL. The ePix10K detectors are expanding the usable range while maintaining a low noise (single photon counting) through the use of different gain modes and auto-ranging [14]. Other gain auto-ranging, hybrid pixel detectors for FELs include Agipd (three gains, optimized for the particular pulse bunching structure of the EuXFEL beam [15]) and Jungfrau (three gains [16]).

The ePix10K cameras are built around modules consisting of a sensor flip-chip bonded to 4 ASICs, resulting in 352×384 pixels of $100 \mu\text{m} \times 100 \mu\text{m}$ each (with a total area of 35.2 mm \times 38.4 mm). They are built on the ePix platform, sharing the hardware and software development with all other cameras built on the same platform [17, 18].

Three ePix10K cameras have been extensively tested with FEL beams at LCLS in the various gain modes, resulting in a measured noise floor of $67 e^-$ ENC (245 eV rms) and a range of 11 000 8 keV photons. We demonstrate the linearity of the response in various gain combinations: fixed high, fixed medium, fixed low, auto-ranging high to low, auto-ranging medium to low, while operating with very low cross-talk, and acquisition rates of up to 480 Hz.

MATERIALS AND METHODS

ePix10K Camera

ePix10K cameras are built around hybrid pixel detector modules obtained by flip-chip bonding 4 ePix10K read-out ASICs [14, 19] to a typical Si sensor (500 μm thick, n-type, resistivity 10 k Ω cm; other options possible) [20]. For increased radiation hardness, the ASIC balconies are protected with high-Z strips [21]. The pixel size is $100 \mu\text{m} \times 100 \mu\text{m}$ and typical module size is 352×384 pixels (35.2 mm \times 38.4 mm). The ePix10K ASICs are designed on the standard ePix platform [17] and the cameras are built on the ePix camera platform [18] which is compatible with the different ePix readout chips. This results in fast development cycles and minimal integration effort with the LCLS data acquisition systems (DAQ), online monitoring (AMI) and offline analysis (psana). In Fig. 1 (a), a typical (vacuum-compatible) ePix camera is shown; (b) depicts the first four ePix10K cameras.

The ePix10K readout ASICs enable high dynamic range imaging by implementing gain auto-ranging, i.e., in each frame, each pixel starts in a higher gain mode; if the pixel signal exceeds a configurable threshold, the pixel switches to a lower gain mode, increasing the range to match the incoming signal (similar to [22, 15, 16]). This enables simultaneously low noise (high gain) acquisition of small signals and high range (low gain) acquisition of large signals, resulting in a dynamic range of 255 eV to 88 MeV. The ePix10K camera has 3 gain modes (high, medium, low), allowing 5 modes of operation (fixed high, fixed medium, fixed low, auto high to low, auto medium to low) which can be configured independently for each pixel. The different modes are summarized in Table 1. Each pixel value yields a 16 bit number, with the first 2 bits identifying the gain mode and the following 14 bits containing the digitized pixel output in the corresponding gain mode. Note the noise approaching 2 analog-to-digital units (ADU) in medium and low gain, which is the expected quantization noise floor due to limited resolution of the analog-to-digital

TABLE 1. ePix10K operating modes and corresponding performance

Gain mode		Gain			Noise			Range (8 keV photons)
		High (ADU)	Medium (ADU)	Low (ADU)	(ADU)	(eV)	(e ⁻)	
FH	Fixed High	132	-	-	3.66	245	67	110
FM	Fixed Medium	-	43	-	2.17	432	118	330
FL	Fixed Low	-	-	1.32	2.00	12 700	3480	11 000
AHL	Auto High to Low	133	-	1.33	4.25	255	70	100/11 000
AML	Auto Medium to Low	-	42	1.32	2.29	466	128	300/11 000

converter (ADC); a higher resolution ADC would enable further improvement of the signal to noise ratio.

The ePix10K operates currently at 480 Hz and offers an upgrade path in several steps to 5 kHz, 25 kHz and 100 kHz, matching the upcoming LCLS-II requirements.

Experimental Setup

The experiments were performed at the MFX beamline at LCLS [23], which is optimized for molecular crystallography. The beam parameters were: photon beam energy 9.5 keV, number of photons per pulse 10^{12} , pulse length 42 fs, repetition rate 120 Hz. The camera integrating time was set to 100 μ s. For the characterization of the different gain modes, flat field calibration and imaging experiments, the cameras were mounted in the horizontal plane at an angle of 90° with the beam (to minimize Compton scattering), and a thin Cu target was placed in the beam, yielding Cu fluorescence (mostly $K\alpha$ at 8.05 keV and a small amount of $K\beta$ at 8.90 keV); see diagram in Fig. 1 (c). The distance between the cameras and the interaction point was 33 mm to achieve an average photon flux of 10^5 photons/pixel/pulse. The average beam intensity was set (or scanned) by using an attenuator with 10 elements, resulting in an average beam intensity of 10^{-2} to 10^5 photons/pixel/pulse. For each attenuator setting, the variations in FEL beam intensity allowed the collection of a range of different intensities. The beam intensity in each pulse was monitored and recorded with 6 beam monitoring diodes deployed at various locations around the cameras. For brevity, we will often quote a photon flux as a number of photons; all measurements in photons express the number of 8 keV photons/pixel/FEL pulse. Throughout the paper, colors indicate the gain mode in which individual measurements were acquired: red represents high gain, green represents medium gain and blue represents low gain.

RESULTS

Gain Calibration and Data Processing

The gain calibration was performed with linear fits of individual pixel outputs as function of the average photon flux (measured with beam monitoring diodes), as indicated by the black line fits in Fig. 2 (b) and (e). In the high and medium gain modes, the gain was also calibrated by fitting the low occupancy histogram (noise peak and first 3 photon peaks) with a pixel charge sharing model, yielding the same results as full-range linear fits (note that ignoring the effects of charge sharing results in biased estimates of peak positions and incorrect gains in any pixel detector).

The data processing at low photon occupancy was performed by dark subtraction, common mode and gain correction, and histogramming. When applicable, single pixel events (i.e., photons depositing most of the charge in a single pixel) were selected from pixel values with signal $> 3\sigma$ and 4 direct neighbors (up, down, left, right) within noise ($< 3\sigma$) in individual frames and histogramming. At high occupancy, the common mode correction and single pixel event selection were not performed. All these operations were implemented with ultrafast Tensorflow algorithms (yielding same results as “classical”, linear programming in 1-2 orders of magnitude shorter time) [24].

A summary of all 5 modes of operation (fixed high, fixed medium, fixed low, auto-ranging high to low, auto-ranging medium to low), with the gains, noise and range results is presented in Table 1. Note that each pixel can be independently configured in a different mode of operation.

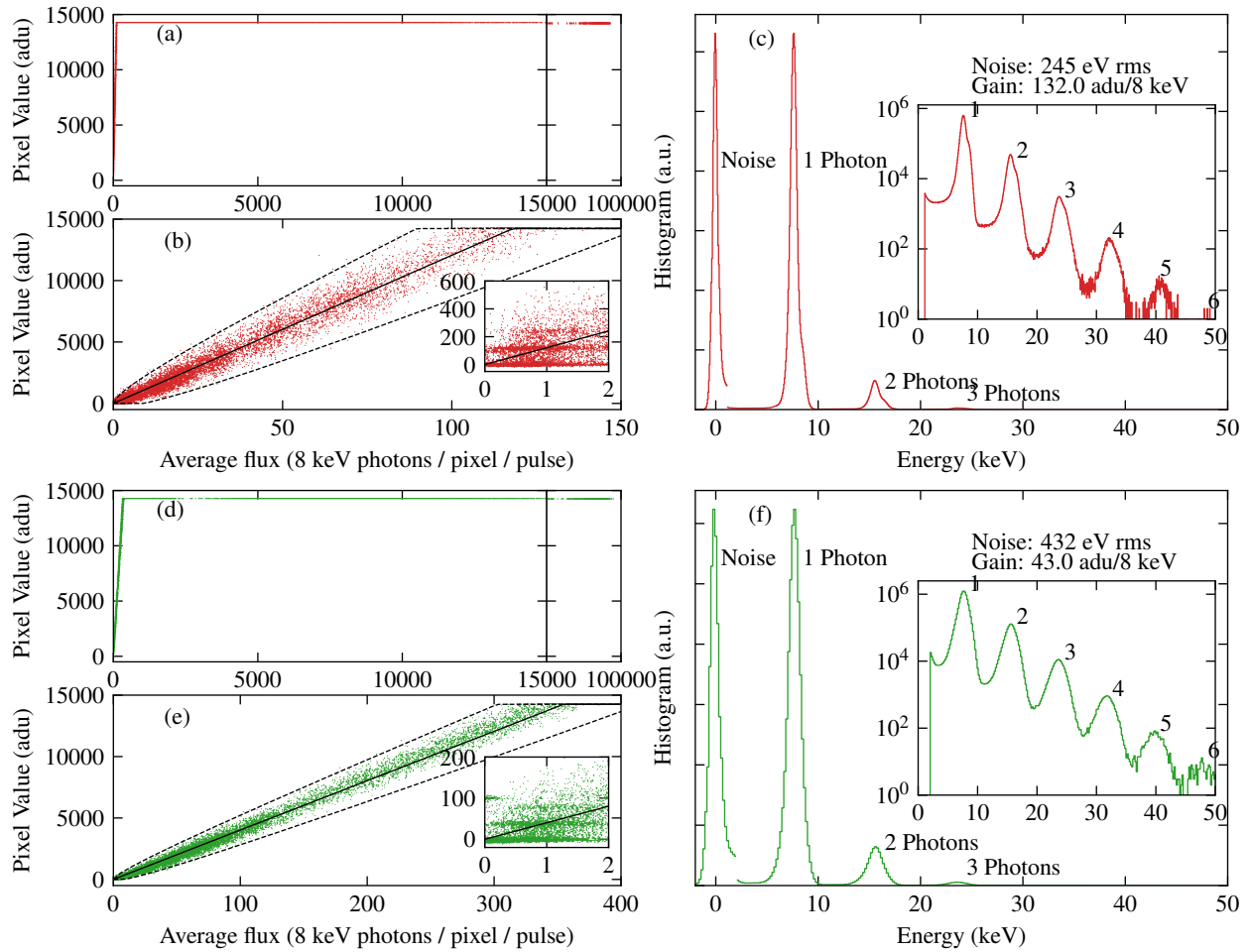


FIGURE 2. Typical behavior of ePix10K camera in fixed high gain mode: (a) and (b) show the response of a single (randomly selected) pixel as a function of the average flux; each dot represents a single frame. (a) Shows the perfect saturation behavior in a range of 0 to 10^5 photons (yielding perfect saturation, despite exceeding the range by a factor 900; note scale change between left and right panel at a flux of 15 000 photons). (b) Displays a close-up of the region up to 0 to 150 photons, demonstrating a range of 110 photons in high gain. The solid black line indicates the linear gain fit and the dashed lines indicate the corresponding Poisson counting statistics (using a stringent $\pm 3\sigma$ noise criterion); note that almost all acquisitions are well within the counting statistics. The inset shows a close-up of the range of 0 to 2 photons. Note the vertical clustering of the dots corresponding to 0, 1, 2, etc. photon signals; also note the linearity over the whole range, with the fitting line passing through (0,0) and (1,1) photons while passing through the center of the acquisitions over the entire range. (c) Depicts the single pixel events spectrum obtained from all pixels in the camera (dark, common mode, gain correction, charge sharing rejection) and, for reference, the noise spectrum (dark and common mode corrected) scaled to match the 1 photon peak height; note the high signal to noise ratio and good peak separation. Inset shows the same on a logarithmic scale, demonstrating clear separation of up to 6 photons (only limited by statistics). Similarly, (d), (e), (f) depict results in fixed medium gain, with similar performance.

Performance in Fixed Gain Modes

In Fig. 2, the typical behavior in the fixed high and medium gain modes is depicted: (a) and (d) show the entire range of 0 to 10^5 photons, demonstrating the perfect saturation response, despite saturation over maximum range by factors of 900 and 300 for high and medium gain, respectively; (b) and (e) demonstrate the linear response of the high and medium gain modes over their entire range (well within the counting statistics bounds indicated by dashed lines), and the insets zoom in to the 0 to 2 photons range where the vertical clustering indicates 0, 1, 2, etc. photons detected; note that the gain fit line passes through the centers of the clusters at the expected locations, demonstrating the consistent

linearity from 1 photon to the full range. For brevity, and because single photons are not visible in the low gain mode, the fixed low gain data is not shown.

Fig. 2 (c) and (f) detail the low light responses of the entire camera in fixed high and medium gain modes, demonstrating uniform responses, high signal to noise ratios and good photon separations up to 6 photons [25] (only limited by the size of the acquired dataset) for both fixed high and fixed medium gain modes. Note that the single pixel events spectrum is obtained from all pixels in the camera (after dark, common mode, gain correction, charge sharing rejection); the noise spectrum (dark and common mode corrected) is shown for reference, scaled to match the 1 photon peak height, resulting in an apparent discontinuity to the right of the noise peak. Note the high signal to noise ratio and good peak separation. The insets show the same data on a logarithmic scale.

The noise is (by definition) the rms width of the noise peak (e.g., 255 eV in high gain); the width of the one photon peak is higher, due to the Fano noise (46 eV at 5.9 keV, added quadratically) and the imperfect gain calibration (due to limited statistics); despite this, the $K\beta$ peak is just barely visible as the asymmetric shoulder to the right of the 1 photon peak in high gain mode (c).

The fixed gain modes offer slightly higher signal to noise ratios ($\sim 4\%$ higher in fixed high gain compared to auto-ranging high to low and $\sim 8\%$ higher in fixed medium gain compared to auto-ranging medium to low) and should be preferred when the range is known to be limited (under 110 photons in high gain and under 330 photon in medium gain). If higher (local or global) pixel intensities are expected, the auto-ranging gain modes are preferable.

Performance in Auto-Ranging Gain Modes

In auto-ranging modes, the high signal to noise ratio is maintained for the high and medium gain (with only modest increases in noise compared to the corresponding fixed gain modes, see previous paragraph; this slight increase in noise reflects a design trade-off between noise and maximum signal at pulsed sources). However, high intensities on individual pixels initiate a gain switch in those pixels, increasing their range to about 11 000 photons. Figure 3 shows the results, which are largely similar to the fixed gain modes shown in Fig. 2; note however the blue dots representing low gain measurements, and the auto-ranging of the gain, taking place at around 90 photons (b) and 270 photons (c). Also note the linear response in high gain, indicated by the matching of the blue dots and the corresponding black fit line.

Because of the large dynamic ranges involved, the auto-ranging behavior between the different gain modes is difficult to show in a linear scale plot; in Fig. 4 we show the auto gain ranging behavior on a log-log plot. (a) depicts the auto-ranging from high to low gain for one (randomly selected) pixel: red dots indicate high gain acquisitions, blue dots indicate low gain acquisitions, and the black line represents the ideal calibrated response. Dashed lines indicate the counting statistics (using a stringent criterion of $\pm 3\sigma$); note that most dots are within the counting statistics. (b) shows the response of the same pixel in the auto-ranging medium to low gain mode, with similar performance. Gain auto-ranging in individual pixels results in small transients; in the most disadvantageous case (shown in Fig. 4), when the entire pixel matrix switches simultaneously, this results in additional noise right after the switching point; this effect will be minimized in the next generation of ePix for high rate applications, ePixHR. However, being able to choose between two different switching points (90 and 270 photons shown here) allows the flexibility to choose the optimal measurement strategy for each experiment.

X-ray Imaging Performance

In Fig. 5, the functionality of the auto-ranging in high to low gain and medium to low gain modes is shown in several usage scenarios. Figure 5 (a) depicts a single, calibrated frame in auto medium to low gain of an illumination field with limited dynamic range (factor 2 in intensity between the brighter area in the top left quadrant and the darker area in the bottom right quadrant) and an average intensity close to the auto-ranging point (270 photons), near the lowest point of signal to noise ratio in this operating mode; note however that the two regions are seamlessly blended.

A high dynamic range scene measured in auto-ranging high to low gain is depicted in Fig. 5 (b) and (c), covering more than 4 orders of magnitude, from single photons behind the most dense areas of the sample to the direct beam of 11 000 photons. (b) Shows a raw image (single frame, pixel ADU values, dark corrected), with the red and blue colors indicating the high and low gain, respectively. The calibrated response (c) shows the seamless integration of the two gain areas, resulting in a high dynamic range image (image shown on a square root scale to facilitate inspection of both bright and dark areas simultaneously).

The limited influence of integration time on the noise performance is shown in Fig. 5 (d); increasing the integration time from 100 μs to 8 ms leads to relatively small increases of the ENC, from 67 e^- to 82 e^- in fixed high gain (red

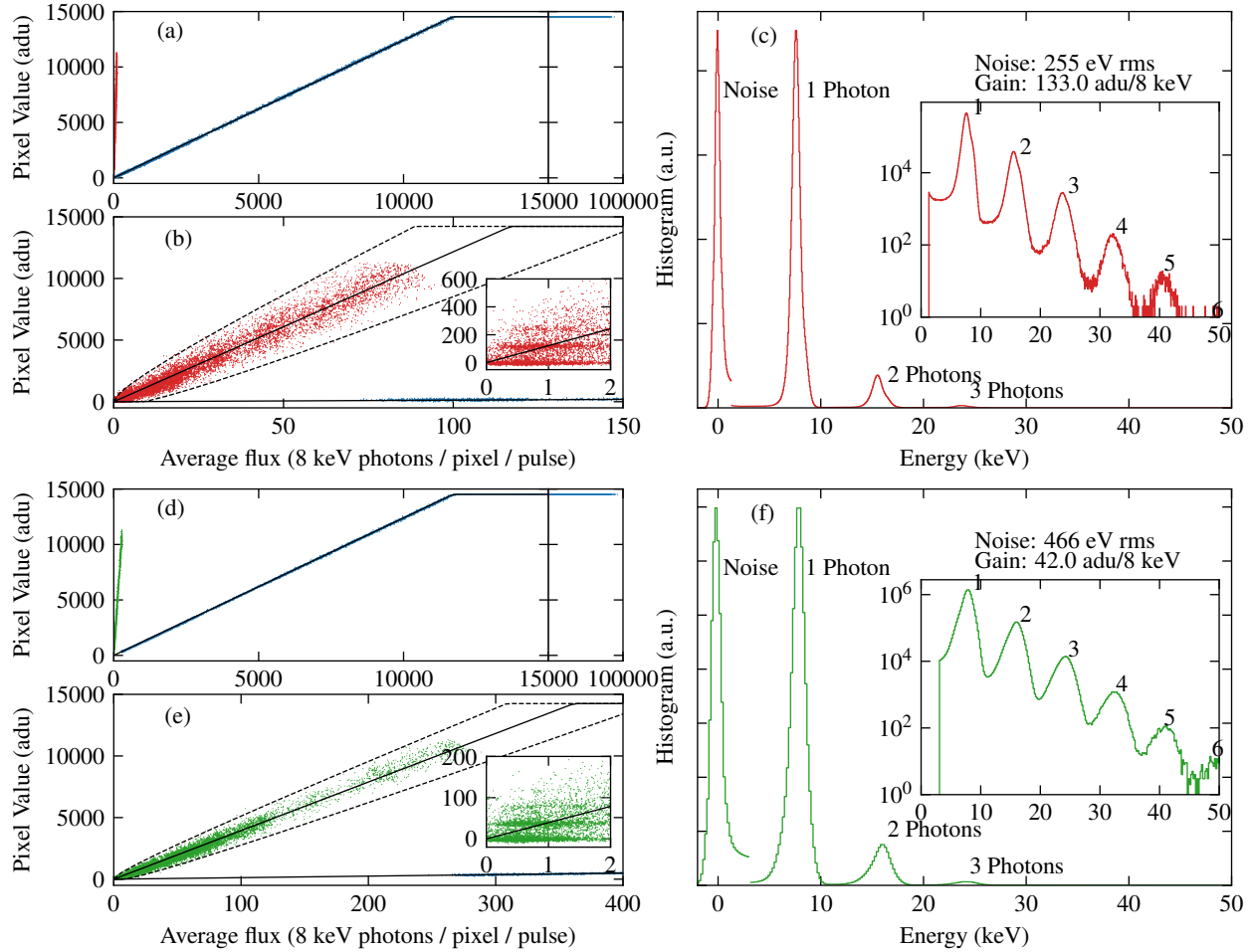


FIGURE 3. Similar results to Fig. 2 for auto ranging gain modes: (a), (b), (c) depict results for auto ranging high to low gain mode, while (d), (e) and (f) show results for auto ranging medium to low. Note the similar performance in high and medium gain, the additional low gain data (blue dots) and their linearity, and the auto ranging points around 90 photons in (b) and 270 photons around (e) for high and medium gain, respectively.

dots) and from $118 e^-$ to $125 e^-$ in fixed medium gain (green dots), enabling efficient detection in, e.g., synchrotron applications [26]; the low gain noise remains essentially unchanged as it is dominated by the ADC quantization noise (not shown in figure).

CONCLUSIONS

The ePix10K cameras have been developed at SLAC to meet demanding detector requirements for LCLS experiments (beyond the capabilities of existing detectors; see an overview in Table 2), while offering an upgrade path towards meeting LCLS-II requirements.

We demonstrated the performance of ePix10K cameras with LCLS beam, showing a low noise floor ($67 e^-$ ENC or 245 eV rms), performance and linearity in the 5 operation modes (fixed high, fixed medium, fixed low, auto-ranging high to low, and auto-ranging medium-to-low, configurable pixel by pixel), correct auto-ranging behavior and tolerance to photon fluxes exceeding the maximum range by up to 900 times.

Achieving this high performance with only one auto-ranging switch (i.e., two gains) leads to relatively simple calibration and reconstruction procedures (compared to, e.g., [27, 28]). The low noise levels allow usage with long integration times at non-FEL sources. Finally, we presented examples of high dynamic range x-ray imaging spanning

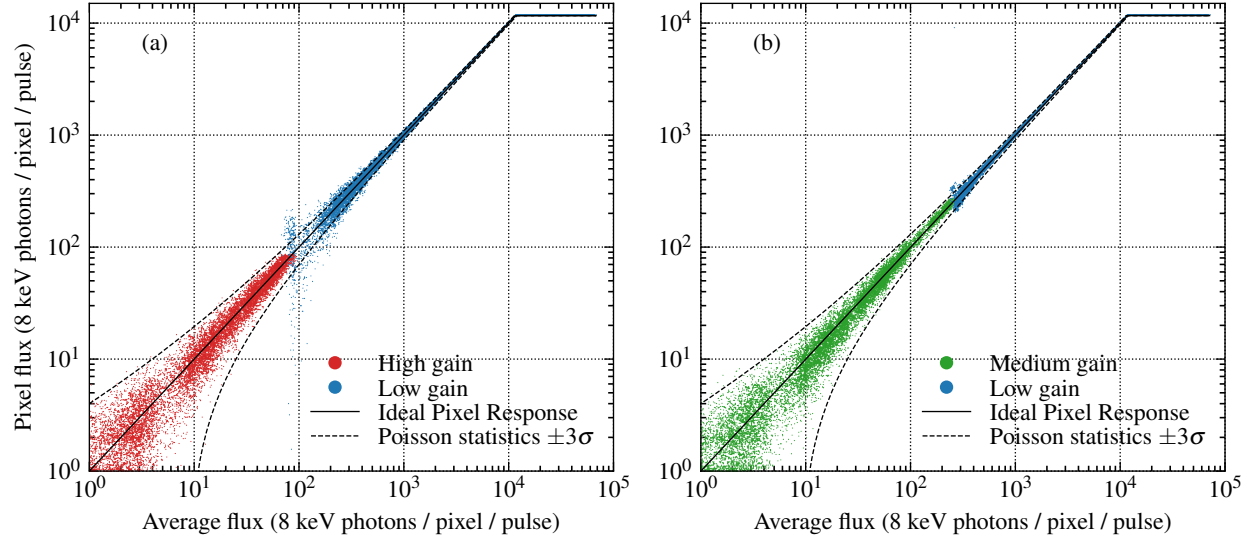


FIGURE 4. ePix10K gain auto-ranging allows an ultra high dynamic range, with a noise of 245 eV rms ($67 e^-$ ENC) and range of 11 000 8 keV photons; (a), (b) display the calibrated response of a single pixel as a function of average beam flux (measured with a separate beam monitoring diode) over > 4 orders of magnitude (log-log scale); red, green and blue dots represent high, medium and low gain measurements, respectively; the black line represents the ideal response; this demonstrates correct auto-ranging behavior, with good linearity and well within the photon counting limits (indicated by black dashed lines, using a stringent noise criterion of $\pm 3\sigma$) over most of the range.

TABLE 2. Overview of SLAC detectors

	ePix10K	ePix100	ePixS	CSPAD low / high gain
Summary	high dynamic range	low noise, deployed	spectroscopic	legacy, deployed
Mode of Operation	2 gains, auto-ranging	1 gain	1 gain	2 gains, fixed
Range (8 keV photons)	11 000	100	10	350 / 2700
Pixel size	$100 \mu\text{m} \times 100 \mu\text{m}$	$50 \mu\text{m} \times 50 \mu\text{m}$	$500 \mu\text{m} \times 500 \mu\text{m}$	$110 \mu\text{m} \times 110 \mu\text{m}$
Module size (pixels)	352×384	704×768	20×20	370×388
Noise (e^- ENC)	$67 e^-$	$43 e^-$	$8 e^-$	$300 e^- / 1000 e^-$

more than 4 orders of magnitude dynamic range (from single photons to 11 000 photons/pixel/pulse).

ePix10K cameras are relatively inexpensive, leveraging the advantages of hybrid pixel detectors with high production yield and good availability. They are modular, easy to scale and integrate [4] and offer an upgrade path in several steps to 5 kHz, 25 kHz and 100 kHz.

ACKNOWLEDGMENTS

Use of the Linac Coherent Light Source (LCLS), SLAC National Accelerator Laboratory, is supported by the U.S. Department of Energy, Office of Science, Office of Basic Energy Sciences under Contract No. DE-AC02-76SF00515. Publication number SLAC-PUB-17275.

REFERENCES

1. P. Emma, R. Akre, J. Arthur, R. Bionta, C. Bostedt, J. Bozek, A. Brachmann, P. Bucksbaum, R. Coffee, F.-J. Decker, Y. Ding, D. Dowell, S. Edstrom, A. Fisher, J. Frisch, S. Gilevich, J. Hastings, G. Hays, P. Hering, Z. Huang, R. Iverson, H. Loos, M. Messerschmidt, A. Miahnahri, S. Moeller, H.-D. Nuhn, G. Pile, D. Ratner,

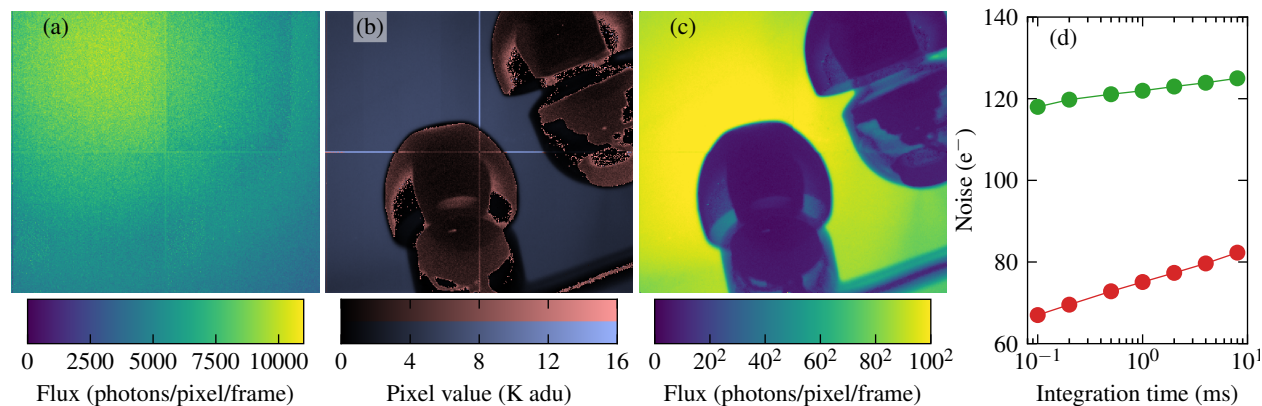


FIGURE 5. ePix10K imaging and long integration noise results: (a) shows a single frame in auto-ranging medium to low gain and calibrated response; 66% of the pixels are in low gain (top left corner) and the remaining pixels are in high gain, however, the two regions blend smoothly; (b) Displays the raw camera response (single frame, dark corrected) in auto-ranging high to low gain mode while imaging a pair of earbuds, with pixels behind dense image areas receiving a lower flux and reading out in high gain (red color), while pixels in the direct beam or behind thinner sample parts switched to low gain mode (blue color); (c) shows the corresponding calibrated response on a square root scale; note the high dynamic range (more than 4 orders of magnitude from single photons in the most dense sample areas to 11 000 photons in the direct beam). (d) Depicts the limited influence of integration time on noise performance: increasing the integration time from 100 μ s to 8 ms only modestly increases the equivalent noise charge, from 67 e^- to 82 e^- in fixed high gain (red dots) and from 118 e^- to 125 e^- in fixed medium gain (green dots), enabling efficient detection in, e.g., synchrotron applications.

- J. Rzepiela, D. Schultz, T. Smith, P. Stefan, H. Tompkins, J. Turner, J. Welch, W. White, J. Wu, G. Yocky, and J. Galayda, *Nature Photonics* **4**, 641–647 (2010).
- D. Pile, *Nature Photonics* **5**, 456–457 (2011).
 - H. Graafsma, *Journal of Instrumentation* **4**, p. P12011 (2009).
 - G. Blaj, G. Carini, S. Carron, G. Haller, P. A. Hart, J. Hasi, S. Herrmann, C. J. Kenney, J. Segal, C. A. Stan, and A. Tomada, *IEEE Transactions on Nuclear Science* **63**, 1818–1826 June (2016).
 - A. Koch, M. Kuster, J. Sztuk-Dambietz, and M. Turcato, *Journal of Physics: Conference Series* **425**, p. 062013 (2013).
 - R. Schoenlein *et al.*, *New science opportunities enabled by LCLS-II X-ray lasers* (SLAC Report, 2015) SLAC-R-1053.
 - P. A. Hart, S. Boutet, G. Carini, M. Dubrovin, B. Duda, D. Fritz, G. Haller, R. Herbst, S. Herrmann, C. J. Kenney, *et al.*, “The CSPAD megapixel X-ray camera at LCLS,” in *SPIE Optical Engineering+ Applications* (International Society for Optics and Photonics, 2012), pp. 85040C–85040C.
 - S. Herrmann, G. Blaj, G. A. Carini, A. Dragone, D. Freytag, G. Haller, P. A. Hart, R. Herbst, C. J. Kenney, L. Manger, *et al.*, “CSPAD upgrades at LCLS,” in *2013 IEEE Nuclear Science Symposium and Medical Imaging Conference (2013 NSS/MIC)* (IEEE, 2013), pp. 1–4.
 - G. Blaj, P. Caragiulo, G. Carini, S. Carron, A. Dragone, D. Freytag, G. Haller, P. A. Hart, R. Herbst, S. Herrmann, J. Hasi, C. J. Kenney, B. Markovic, K. Nishimura, S. Osier, J. Pines, J. Segal, A. Tomada, and M. Weaver, *Synchrotron Radiation News* **27**, 14–19 (2014).
 - G. Blaj, P. Caragiulo, G. Carini, S. Carron, A. Dragone, D. Freytag, G. Haller, P. Hart, J. Hasi, R. Herbst, S. Herrmann, C. J. Kenney, B. Markovic, K. Nishimura, S. Osier, J. Pines, B. Reese, J. Segal, A. Tomada, and M. Weaver, *Journal of Synchrotron Radiation* **22**, 577–583 (2015).
 - G. Blaj, P. Caragiulo, G. Carini, A. Dragone, G. Haller, P. Hart, J. Hasi, R. Herbst, C. J. Kenney, B. Markovic, K. Nishimura, J. Pines, J. Segal, C. Tamma, and A. Tomada, *AIP Conference Proceedings* **1741**, p. 040012 (2016).
 - G. Blaj, P. Caragiulo, A. Dragone, G. Haller, J. Hasi, C. J. Kenney, M. Kwiatkowski, B. Markovic, J. Segal, and A. Tomada, *SPIE Proceedings* **9968**, 99680J–99680J–10 June (2016).

13. G. A. Carini, R. Alonso-Mori, G. Blaj, P. Caragiulo, M. Chollet, D. Damiani, A. Dragone, Y. Feng, G. Haller, P. Hart, J. Hasi, R. Herbst, S. Herrmann, C. J. Kenney, H. Lemke, L. Manger, B. Markovic, A. Mehta, S. Nelson, K. Nishimura, S. Osier, J. Pines, B. Reese, A. Robert, J. Segal, M. Sikorski, S. Song, J. Thayer, A. Tomada, M. Weaver, and D. Zhu, *AIP Conference Proceedings* **1741**, p. 040008 (2016).
14. P. Caragiulo, A. Dragone, B. Markovic, R. Herbst, K. Nishimura, B. Reese, S. Herrmann, P. Hart, G. Blaj, J. Segal, A. Tomada, J. Hasi, G. Carini, C. J. Kenney, and G. Haller, "Design and characterization of the ePix10k prototype: A high dynamic range integrating pixel ASIC for LCLS detectors," in *2014 IEEE Nuclear Science Symposium and Medical Imaging Conference (NSS/MIC)* (IEEE, 2014), pp. 1–3.
15. B. Henrich, J. Becker, R. Dinapoli, P. Goettlicher, H. Graafsma, H. Hirsemann, R. Klanner, H. Krueger, R. Mazzocco, A. Mozzanica, H. Perrey, G. Potdevin, B. Schmitt, X. Shi, A. K. Srivastava, U. Trunk, and C. Youngman, *Nuclear Instruments and Methods in Physics Research Section A: Accelerators, Spectrometers, Detectors and Associated Equipment* **633**, S11 – S14 (2011), 11th International Workshop on Radiation Imaging Detectors (IWORID).
16. A. Mozzanica, A. Bergamaschi, S. Cartier, R. Dinapoli, D. Greiffenberg, I. Johnson, J. Jungmann, D. Maliakal, D. Mezza, C. Ruder, *et al.*, *Journal of Instrumentation* **9**, p. C05010 (2014).
17. A. Dragone, P. Caragiulo, B. Markovic, R. Herbst, B. Reese, S. C. Herrmann, P. A. Hart, J. Segal, G. Carini, C. J. Kenney, and G. Haller, "ePix: a class of architectures for second generation LCLS cameras," in *Journal of Physics: Conference Series*, Vol. 493 (IOP Publishing, 2014) p. 012012.
18. K. Nishimura, G. Blaj, P. Caragiulo, G. Carini, A. Dragone, G. Haller, P. Hart, J. Hasi, R. Herbst, S. Herrmann, C. J. Kenney, M. Kwiatkowski, B. Markovic, S. Osier, J. Pines, B. Reese, J. Segal, A. Tomada, and M. Weaver, *AIP Conference Proceedings* **1741**, p. 040047 (2016).
19. P. A. Hart, G. Blaj, P. Caragiulo, G. Carini, A. Dragone, G. Haller, J. Hasi, R. Herbst, S. Herrmann, C. J. Kenney, H. Lemke, B., S. Nelson, K. Nishimura, S. Osier, J. Pines, B. Reese, J. Segal, A. Tomada, M. Weaver, and D. Zhu, "Characterization of the ePix10k X-ray camera at SSRL and LCLS," in *2014 IEEE Nuclear Science Symposium and Medical Imaging Conference (NSS/MIC)* (IEEE, 2014), pp. 1–4.
20. G. Blaj, J. Segal, C. Kenney, and G. Haller, (2017), arXiv:1706.01429 [physics.ins-det], arXiv:1706.01429 [physics.ins-det].
21. A. Tomada, S. Boutet, B. Duda, P. Hart, C. J. Kenney, L. Manger, M. Messerschmidt, J. Tice, and G. Williams, "High-Z radiation shields for X-ray free electron laser detectors," in *Nuclear Science Symposium and Medical Imaging Conference (NSS/MIC), 2012 IEEE* (IEEE, 2012), pp. 511–514.
22. D. Freytag, R. Herbst, J. Brau, M. Breidenbach, R. Frey, G. Haller, B. Holbrook, R. Lander, T. Nelson, V. Radeka, D. Strom, and M. Tripathi, "Kpix, an array of self triggered charge sensitive cells generating digital time and amplitude information." in *2008 IEEE Nuclear Science Symposium Conference Record* (IEEE, 2008), pp. 3447–3450.
23. S. Boutet, A. E. Cohen, and S. Wakatsuki, *Synchrotron radiation news* **29**, 23–28 (2016).
24. G. Blaj, C.-E. Chang, and C. Kenney, *AIP Conference Proceedings* **2054**, p. 060077 (2019).
25. G. Blaj, C. Kenney, A. Dragone, G. Carini, S. Herrmann, P. Hart, A. Tomada, J. Koglin, G. Haller, S. Boutet, M. M. G. Williams, M. Chollet, G. Dakovski, S. Nelson, J. Pines, S. Song, and J. Thayer, *IEEE Transactions on Nuclear Science* **64**, 2854–2868 (2017).
26. G. Blaj, D. Bhogadi, C.-E. Chang, D. Doering, C. Kenney, T. Kroll, J. Segal, D. Sokaras, and G. Haller, *AIP Conference Proceedings* **2054**, p. 060037 (2019).
27. D. Mezza, A. Allahgholi, A. Delfs, R. Dinapoli, P. Goettlicher, H. Graafsma, D. Greiffenberg, H. Hirsemann, A. Klyuev, T. Laurus, *et al.*, *Journal of Instrumentation* **11**, p. C11019 (2016).
28. S. Redford, M. Andrä, R. Barten, A. Bergamaschi, M. Brückner, R. Dinapoli, E. Fröjdth, D. Greiffenberg, C. Lopez-Cuenca, D. Mezza, *et al.*, *Journal of Instrumentation* **13**, p. C01027 (2018).